Unveiling Microstructure-Property Correlations in Nuclear Materials with High-energy Synchrotron X-ray Techniques

Xuan Zhang[a,*]

[a] *Nuclear Science and Engineering Division, Argonne National Laboratory, Lemont, IL USA 60439*

** Corresponding author, xuanzhang@anl.gov, 9700 South Cass Avenue, Lemont, IL USA 60439*

Abstract

Understanding the microstructure-property correlation is critical for the performance evaluation of in-service materials and the development of advanced materials for nuclear reactor applications. Experimental studies are challenging for nuclear materials which are often hazardous. Recent developments in high-energy synchrotron X-ray (HEX) techniques offer the potential to address this challenge, by providing direct observations of internal responses to external stimuli in bulk-like materials, through *in situ* or 3D measurements. In this review, developments in HEX techniques are introduced and recent applications in nuclear materials are presented. The results offer unprecedented insights into materials performance and provide unique input to computational models.

Keywords

Wide-angle X-ray scattering; high-energy X-ray diffraction microscopy; X-ray tomography; *in situ* techniques; non-destructive examination

1. Introduction

The breadth of material systems used in nuclear reactors, coupled with the harsh environments, poses extensive challenges to the understanding and prediction of materials performance in service [1]. A significant fraction of nuclear materials are radioactive, bringing additional challenges to their acquisition, handling, and investigation. Currently, the study of nuclear materials often separates the microstructural characterization from testing, making a direct microstructure-property correlation difficult. One approach that couples the two is the small-scale testing inside electron microscopes, enabling the tracking of microstructure with deformation. This is particularly helpful in studying ion irradiated materials since the irradiation depth is shallow [2]. However, the extrapolation of results from small-scale testing to bulk materials performance suffers from the size effects [3].

High-energy synchrotron X-rays (HEX), which generally refers to X-rays of energies ≥30 keV, have a high penetrating power that can be utilized to non-destructively measure internal microstructural features in up to 3 dimensions (3D) in bulk materials. In recent years, HEX have been increasingly used for nuclear materials research, owing to the advancements in several aspects: 1) high-energy X-ray beamlines have become standard in the third and the fourth generation synchrotron light sources; 2) the techniques are matured; 3) notable efforts have been made to enable the study of hazardous nuclear materials at public beamlines (for example, see [4-6]), and to facilitate the access to beamlines by the nuclear community (for example, see the Nuclear Science User Facilities [7]); 4) the attractive scientific merit in non-destructively tracking the bulk materials' response in simulated reactor environments *in situ* and/or in 3D.

This review highlights some advancements, mostly taken place since 2017, in unveiling the microstructure-property correlation in nuclear materials via HEX techniques, in particular the *in situ* and 3D techniques. The techniques covered include wide-angle X-ray scattering (WAXS, also known as HEXRD for high energy X-ray diffraction), small-angle X-ray scattering (SAXS), high-energy X-ray diffraction microscopy (HEDM, also known as 3DXRD for 3D X-ray diffraction microscopy), and X-ray computed

microtomography (μCT). The case studies presented here cover a wide range of materials from graphite to structural/cladding alloys to uranium fuels, many of which have been exposed to neutron irradiation. During the X-ray measurements, some of the materials were subjected to external stimulations, such as stress, temperature, or corrosion. The rich information obtained from these studies offers unprecedented insights into the microstructure-property correlation, and serves as valuable inputs for improving computational models. In addition to highlighting on-going developments, a glimpse into future possibilities is provided.

2. Wide-angle X-ray scattering (WAXS) and small-angle X-ray scattering (SAXS)

Figure 1a shows the absorption length (1/*e* distances) in elemental solids for five different photon energies. It is readily seen that X-rays with energies ≥70 keV can penetrate ≥1 mm through many materials used for nuclear applications including Fe, Ni, and Zr. For heavier elements such as W and U, penetration depths are still significant at ~100 μm. Such high penetration power enables HEX measurements to be carried out typically with a transmission geometry (Figure 1b). Coherent scattering angles are small as per Bragg's law $2d\sin\theta = \lambda = 12.3984/E$, where d is the lattice spacing in Angstroms, θ is the scattering angle, λ is the wavelength in Angstrom, and E is the x-ray energy in keV. A 100 keV photon beam has a θ angle of only 4.8° for the 9th peak {422} of an austenitic stainless steel with a nominal lattice constant of 3.6 Å. Such small diffraction angles facilitate the use of two-dimensional (2D) area detectors, and enable the use of many sample containments as they require only small openings, such as furnaces and environmental chambers. The ample space between the sample and the detector, often one to several meters, also makes room for complex experimental setups, including the containments needed for radiological control.

Another salient aspect with HEX at synchrotron sources is the high brightness, making the data collection very fast, typically in a fraction of a second for one exposure. This enables *in situ* measurements over a series of steps in time, deformation, temperature, etc.. For dynamic processes that span a few hours, hundreds to thousands of measurement points can be obtained to track the microstructural changes.

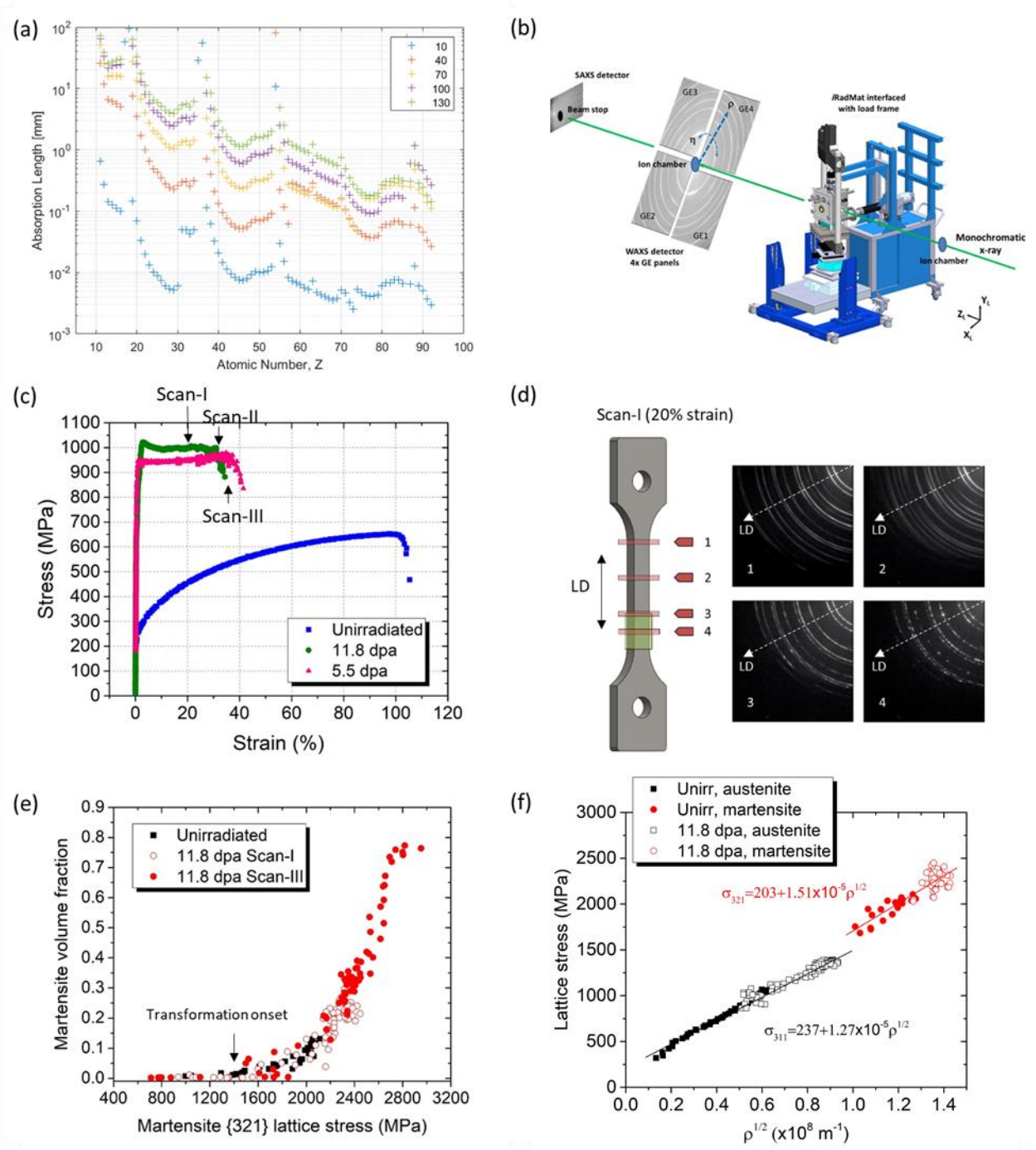

Figure 1. (a) Absorption length in elemental solids spanning the periodic table for five different photon energies in the hard X-ray regime. The numbers in the caption are photon energies in keV. The data were based on absorption coefficients from National Institute of Standards and Technology Reference Database 126, and the figure were plotted using the MATLAB toolbox [8]. (b) Illustration of the simultaneous WAXS/SAXS measurement setup at beamline 1-ID of the Advanced Photon Source with the *i*RadMat experimental module. Reproduced from Reference [4]. (c) The engineering stress-strain curves of the unirradiated, the 320 °C/11.8 dpa irradiated, and the 320 °C/5.5 dpa irradiated 316 stainless steel samples during RT tensile tests. (d) Snapshots from an area detector showing the diffraction patterns at selected locations along the 11.8-dpa sample gauge in Scan-I (20% strain); loading direction (LD) is marked on each pattern. (e) Martensite volume fraction as a

function of the martensite {321} stress for the unirradiated and the 11.8-dpa irradiated samples. (f) Lattice stress as a function of square-root of dislocation density in the unirradiated and the 11.8 dpa irradiated samples. The stress for the austenite is the {311} stress, and the stress for the martensite is the {321} stress. Subfigures (c), (d), (e) and (f) are reproduced from Reference [9].

The scattering signals from X-rays passing through the sample can be divided into wide angle and small angle ranges, corresponding to the WAXS and SAXS techniques, respectively. Figure 1b illustrates a unique setup at the beamline 1-ID of the Advanced Photon Source (APS) that enables the simultaneous recording of WAXS and SAXS patterns during an *in situ* loading/heating of activated materials. WAXS generally refers to the analysis of the Bragg peaks which contain crystallographic information, while SAXS is the analysis of the scattering signal around the transmitted beam which contains information about the nano- to micro- scale electron density differences within the sample. SAXS has been used to track the evolution of deformation voids in nuclear structural alloys [10] and to characterize the nanoscale intermetallic precipitates in highly neutron irradiated reactor pressure vessel steels [11] at high energy beamlines, but in general, dedicated SAXS beamlines use lower energies (typically 10-30 keV) to obtain an optimum Q range coverage, and therefore, it is not discussed further in this review.

WAXS has been broadly employed to study polycrystalline nuclear materials due to the relatively simple setup and well-developed data processing methodologies. WAXS provides rich microstructural information including crystallite phase identification and volume fractions, internal strains, intra-phase chemical composition, crystallite sizes, defect densities, and short range ordering (for amorphous phases). Some of this information can be ascertained directly from WAXS data and others requires some level of modelling. In recent years, research using high-energy WAXS has covered a broad range of topics in nuclear materials, including irradiation effects, mechanical performance, thermal response, corrosion performance and materials processing. Many of them are *in situ* studies, owing to the development of enabling infrastructures at beamlines. Recently, we developed an *in situ* Radiated Materials (*i*RadMat) experimental module at the Advanced Photon Source beamline 1-ID that allows *in situ* WAXS/SAXS studies of radioactive samples subject to thermo-mechanical loading [4]. Figure 1b shows the schematic of the *i*RadMat module during the *in situ* measurement. The core of this module was a radiation-shielded vacuum furnace with the sample rotation-under-load capability. The furnace was designed to interface with a servo-hydraulic load frame for tensile loading of the sample. Incident and diffracted high-energy X-rays passed through quartz windows. The first study using the *i*RadMat is a study of the neutron-irradiation effect on the tensile properties of a Fe-9%Cr alloy [12]. Two neutron-irradiated specimens, one irradiated at 300 °C to 0.01 dpa and the other at 450 °C to 0.01 dpa, were tested at the room temperature (RT) along with an unirradiated counterpart. The evolutions of the lattice strains, the dislocation densities and the coherent scattering domain sizes during deformation revealed different roles of the submicroscopic defects in the 300 °C/0.01 dpa specimen and the nanometer-sized dislocation loops in the 450 °C/0.01 dpa specimen; the dislocation loops were more effective in retarding the dislocation glide. While the work hardening rate of the stage II deformation was unaffected by irradiation, significant dynamic recovery in the stage III deformation in the irradiated specimens led to the early onset of necking without the stage IV deformation that had been observed in the unirradiated specimen.

In a separate study using the *i*RadMat module, we [9] observed that during RT tensile tests, 320 °C/5.5 dpa and 320 °C/11.8 dpa neutron-irradiated Type 316 stainless steel samples developed unusual deformation bands propagating along the sample gauge, similar in appearance to a Lüders band, leading to a combined high strength and high ductility (Figures 1c and 1d). With the help of *in situ* WAXS, we discovered that the increased yield strength of the irradiated material compared to the unirradiated material (Figure 1c) promoted the martensitic phase transformation. The martensitic transformation served as a hardening mechanism in addition to the dislocation hardening, leading to a reduced tendency towards localized

deformation in the irradiated material. The results also showed that the irradiation did not alter the dislocation hardening and the martensitic transformation mechanisms (Figures 1e and 1f), but the increased yield strength in irradiated materials facilitated the localized phase transformation at the onset of plastic deformation, in contrast to the unirradiated material which required pre-straining.

We also performed a high-temperature *in situ* study using the *i*RadMat module on an irradiated high-temperature-ultra-fine-precipitation-strengthened (HTUPS) stainless steel [13]. The tensile deformation behavior of two 400°C/3dpa irradiated samples were studied at RT and at 400°C, respectively. We discovered that the evolution of the {200} lattice strain corresponds well with the dislocation density evolution, and is an effective probe of the deformation-induced long-range internal stresses that are related to the irradiation-induced defects.

In recent years, many other researchers have used high-energy WAXS to unveil the irradiation effects. Koyanagi et al. [14] used *ex situ* WAXS and measured strips of SiC that experienced irradiation creep under flexural stress. They found a correlation between the increase in the (111) shoulder peak intensity and the accumulation of the nano-scale stacking disordering due to the applied stress under irradiation, and proposed a transient creep mechanism. Simos *et al.* [15] used *ex situ* WAXS to study the proton-irradiation-induced damage in a graphite target. The WAXS patterns revealed the extent of the irradiation beam that caused the transformation of the graphite lattice structure to nanocrystalline, and also revealed the role of the irradiation temperature profile. *In situ* WAXS has been used to study a variety of mechanical or thermal modalities in conventional or novel nuclear materials including fuels. Laliberte et al. [16] studied the creep deformation in a Grade 91 steel at 650°C, and correlated the creep stages with the dislocation density evolution. Vakhitova et al. [17] studied the texture evolution related to the phases transformations in an ODS ferritic steel during heating cycles, and observed a texture memory effect that is dependent on the cooling rate and an invariant crystallite size in all phases likely due to the pinning effect of dispersion particles. Shiman et al. [18] studied the strain evolution due to thermal-cycling-induced hydride dissolution and precipitation in a CANDU Zr-2.5 wt% Nb tube material, and discovered the variations in the hydrostatic and deviatoric strain components of the α-Zr matrix with temperature through detailed examination of the WAXS patterns. Miao et al. [19] studied the microstructural evolution in a ultrasonic additive manufactured (AM) Zr under RT tensile testing, and identified the stress concentration sites during early stage of plastic deformation, which may be correlated with the manufacturing defects and become candidate necking locations. We [20] studied the room temperature tensile behavior of an AM316L stainless steel manufactured by the laser powder bed fusion (LPBF), and identified the difference in deformation stages in AM material compared to the conventional material. Sprouster et al. [21] examined the *in situ* response of stoichiometric and non-stoichiometric UO_2 during flash sintering and traced the subtle structural changes prior to and post flash, indicating that the stoichiometry and applied parameters could potentially be tailored to optimize the fabrication process for nuclear fuels.

High energy WAXS of other configurations instead of transmission has also been applied to recent nuclear materials research. For corrosion study, grazing incidence diffraction (GID) has been used to probe the thin corroded layer [22, 23]. Microdiffraction (μXRD) has been used to map the surface lattice strains developed in areas with cracks and indents in a micro-indentation tested UO_2 sample [24]. Energy dispersive X-ray diffraction (EDXRD, also known as energy dispersive diffraction, EDD), which utilizes polychromatic X-rays to the high-energy range, has been used to measure the residual stress field in a large weldment obtained from a canceled boiling water reactor [25]. EDXRD has also been used to reveal the lattice change due to proton irradiation in a graphite material [26]. Those studies demonstrated the versatility of WAXS and show cased the broad range of topics within the nuclear materials study.

3. High-energy X-ray diffraction microscopy (HEDM)

HEDM is based on WAXS and is a recent addition to the microscopy family. It uses crystal unit cell orientations as the contrast mechanism to acquire the sizes, locations, orientations, and elastic strain states of individual diffracting volumes in bulk polycrystalline materials nondestructively and in 3D. It is also known as 3DXRD and is implemented at multiple high-energy synchrotron facilities around the world, such as the beamline 1-ID of the APS, the F2 station at the Cornell High Energy Synchrotron Source (CHESS), beamline ID11 of the European Synchrotron Radiation Facility (ESRF), and the P07 and P21 beamlines at the PetraIII Facility. The technique has seen a rapid development over the past decade, motivated by its unprecedented power to reveal grain-level microstructural responses to external stimuli, such as mechanical loading, high temperatures, and irradiation [27, 28]. It also provides direct input to constitutive models for validation or further development [29].

The principle, experimental setup, and data processing of HEDM have been elaborated in a number of recent reviews [30-32]. The technique uses a monochromatic high-energy X-ray beam to illuminate a volume in the sample. The sample is rotated continuously about an axis nominally perpendicular to the incident beam, while 2D area detectors collect diffraction signals at small rotational steps, typically over a small fraction of a degree. The rotation often covers a range of $\Delta\omega = 180$ or 360°. Depending on sample to detector distance $L_{s\text{-}d}$, two variants of the HEDM technique exist, namely the far-field HEDM (ff-HEDM) and near-field HEDM (nf-HEDM). Due to the relative novelty of these techniques in nuclear materials research, they are briefly introduced here.

For ff-HEDM, $L_{s\text{-}d}$ typically ranges from 0.5 to several meters downstream from the sample. Figure 2a illustrates the setup with a double-contained neutron-irradiated radioactive sample in the beam (in this particular case, a Fe-9%Cr tensile sample [28]). ff-HEDM uses a box beam that is typically several hundreds of μm (vertically) by up to several mm (horizontally), with the horizontal size typically matching the sample cross-section. Polycrystalline materials, which may contain hundreds to thousands of grains in this measurement volume, are rotated and the diffraction patterns are recorded as a function of the angle. During data processing, the intensity peaks in the patterns are indexed to each coherent volume (e.g. grain) in the sample, with each grain typically contributing many peaks in the rotation series. The radial position of a diffraction peak is inversely proportional to the d(hkl) spacing, which encodes further information on elastic strain. Furthermore, the relative position of different peaks from a given grain (vs. rotation angle) allows determination of the center of mass position for the grain. The azimuthal broadening or splitting of a peak reflects the presence of orientation gradient or orientation domains in the crystallite, while the radial broadening is a manifestation of the strain gradient. The integrated intensity of the peak is a measure of the diffracting volume. At synchrotron facilities, the ff-HEDM data collection time is approximately 3-15 minutes per layer depending on the scattering power and the desired resolution.

For nf-HEDM, $L_{s\text{-}d}$ typically ranges from 4 to 15 mm. Figure 2b illustrates the setup. nf-HEDM uses a line-focused beam that is just a few μm thick to illuminate a thin layer in the sample. The measurement of one layer usually needs to work with 2 to 3 different $L_{s\text{-}d}$. To map a 3D volume, many layers need to be measured and stacked. Due to the small $L_{s\text{-}d}$, nf-HEDM loses its sensitivity to strain. Instead, a voxel-by-voxel forward-modeling reconstruction converts the set of diffraction images into an orientation map similar to an electron backscatter diffraction (EBSD) image. The voxel size can be as small as 1-3 μm, and the orientation resolution is 0.1°. The nf-HEDM collection time per layer is similar to ff-HEDM, but since smaller layer thickness and spacing are typically used, measuring equivalent 3D volumes take longer (up to hours).

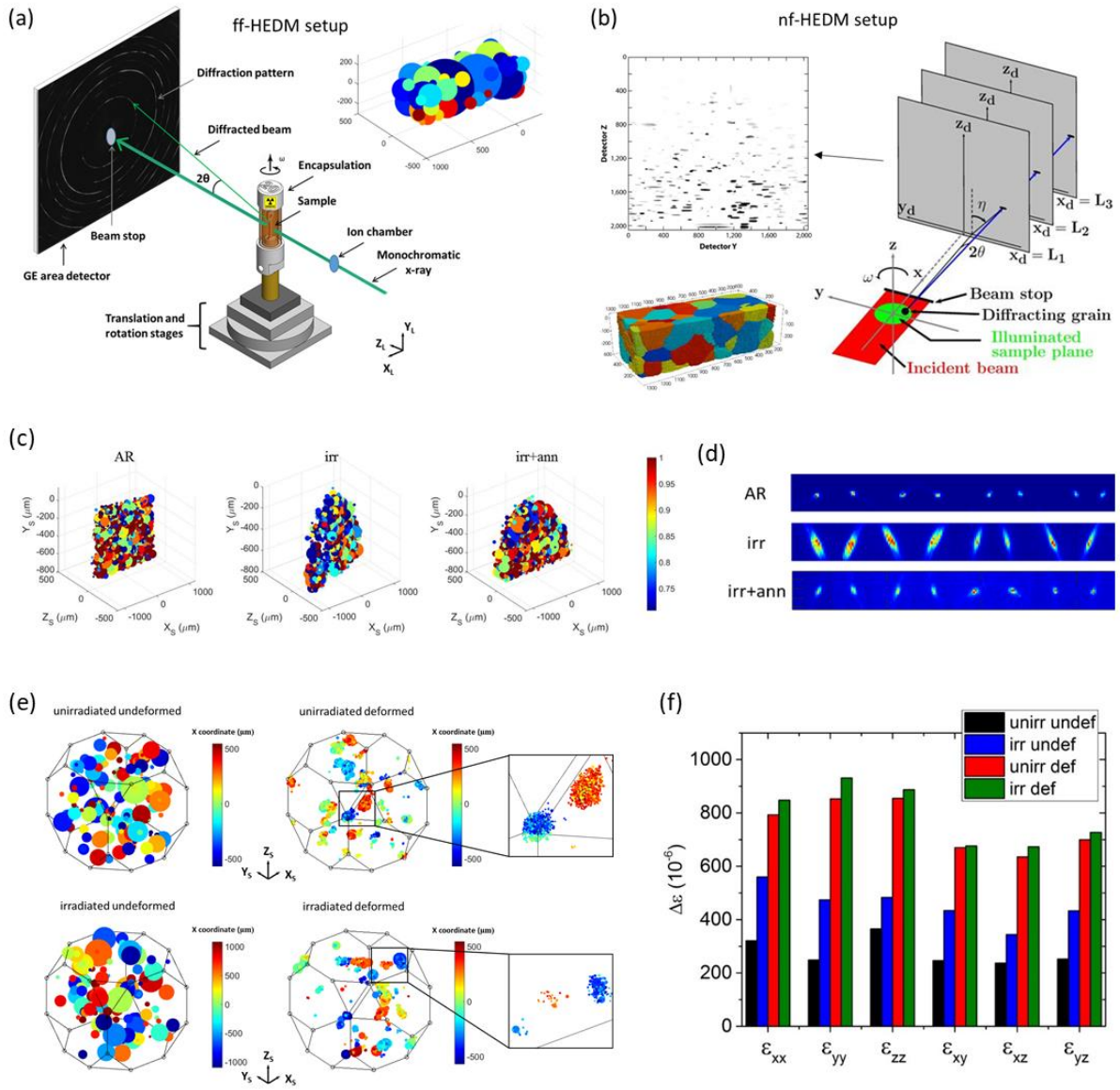

Figure 2. (a) Schematic of ff-HEDM experimental setup for a neutron-irradiated sample reproduced from Reference [28]. The sample is double-encapsulated by kapton tubes. Top right corner shows the reconstruction of grains in an irradiated alloy [unpublished data from the author]. The colors are unique to each grain. (b) Schematic of nf-HEDM experimental setup reproduced from Reference [33]. Bottom left corner shows the reconstruction of grains in the same volume as that in (a), through the stacking of many layers [unpublished data from the author]. The colors are informative of the grain orientations. (c) Center-of-Mass (COM) maps for the as-received (AR) HTUPS stainless steel sample, the 500 °C/3 dpa neutron-irradiated (irr) sample and the irradiated and then annealed (irr + ann) sample. The size of each sphere reflects the size of the grain. The color denotes the reconstruction confidence, from 0.7 to 1. (d) Diffraction spots from the eight {111} reflections of a single grain in each sample. Subfigures (c) and (d) are reproduced from Reference [27]. (e) Domain mapping in the Rodrigues-Frank orientation space for four conditions of a Fe-9%Cr alloy: unirradiated undeformed, unirradiated deformed, irradiated undeformed, and irradiated deformed. The irradiation condition was 450 °C/001 dpa. Each sphere represents a grain/subgrain, size scaled with the volume and color denoting the X-coordinate of the grain in the real space. The two insets on the right shows magnified view of some of the

clustered subgrains. (f) Bar plot of the strain spread for the six strain tensor components in the four materials conditions. Subfigures (e) and (f) are reproduced from Reference [28].

The meso-scale, grain-level structural information provided by HEDM fills the gap between the macroscopic properties and the nano- or μm-scale microstructures characterized by other microscopy techniques such as electron microscopy. It provides quantitative information of the internal heterogeneity in a material's microstructural evolution, through *in situ* or *ex situ* measurements. In nuclear materials field, a pioneering work by Abdolvand et al. in 2015 [34] used *in situ* ff-HEDM to study the deformation twinning under a tensile load in a polycrystal Zircaloy-2. The investigation volume contained 6132 grains prior to deformation, and at the last loading step (2.79% macro-strain), 9724 grains were identified as a result of twinning. The authors used an algorithm to pair the twins with parent grains, resulting in 1079 twins paired to 342 parents, enabling high-fidelity statistical analysis of 3D stress state. The results showed significance in the influence of neighboring grains on the twinning behavior of either plastically "soft" or "hard" grains. In a separate paper by the same group of authors [35], the crystal plasticity finite element (CPFE) simulation was employed to study the stress heterogeneity within each individual grain of a polycrystal Zircaloy-2 material, using the ff-HEDM reconstruction as the input microstructure. The agreement between the simulation and the experiment shed a light on the parent-twin interactions in hcp materials.

In recent years, we focused on the investigation of microstructural changes in neutron-irradiated samples with ff-HEDM. In an earlier work, we [27] presented the first study of the effect of neutron irradiation and post-irradiation annealing on the grain structures using ff-HEDM. A 500 °C/3 dpa irradiated HTUPS stainless steel sample and a 500 °C/3 dpa irradiated + 600 °C/1 h annealed sample were double-encapsulated with Kapton tubes and placed in the beam for subsequent measurement (Figure 2a), followed by an unirradiated counterpart. The study shows that irradiation caused significant reduction in grain reconstruction confidence (Figure 2c), increased the individual diffraction spot broadening (Figure 2d), modified the texture, among some others, but had nearly no effect on the average grain size and grain size distribution. Post-irradiation annealing largely reversed the irradiation effects on texture and average lattice constant, but inadequately restored the microstrain.

We [28] also used ff-HEDM to measure the grain structures in the tensile-deformed neutron-irradiated sample following the *in situ* WAXS study in Reference [12]. Two locations were probed on the deformed sample: in the grip area where no plastic deformation occurred, and in the gauge area where uniform deformation occurred. Similar measurement was also performed in the unirradiated counterpart. We found that in similar volumes, the undeformed areas contained ~150 grains, while the deformed area had 3425 and 1283 grains identified for the unirradiated and the 450 °C/0.01 dpa irradiated samples, respectively, due to the formation of subgrains upon deformation (Figure 2e). The irradiated sample showed greater heterogeneity in the subgrain formation compared to the unirradiated sample. We also found that while the irradiation broadened the residual strain distribution in the undeformed state, tensile deformation to failure resulted in similar residual strain distributions between the irradiated and the unirradiated samples (Figure 2f).

nf-HEDM has been used by Hanson et al. [36] in a study of hydrogen-assisted cracking in Ni-based alloy 725. Coupled with X-ray μCT (to be discussed in the next section), the authors investigated the relationship between the crystallographic character of grain boundaries and their susceptibility to hydrogen-assisted crack propagation. They found that grain boundaries with low-index planes (BLIPS) are most resistant to cracking, paving the way for better predicting the service lifetime of structural components, as well as for designing new HE-resistant materials via grain boundary engineering. nf-HEDM coupled with μCT has also been used in the characterization of as-sintered UO_{2+x} nuclear fuels [37]. For such a high-Z material, the authors used 85 keV X-rays and measured nominally 0.35 × 0.35 mm^2 cross sectional areas with an in-

plane resolution of ~ 3 μm, pushing the resolution limit for both nf-HEDM and μCT. They characterized the grain size distribution and the grain boundary misorientations, and observed increased sintering kinetics for hyper-stoichiometric samples. These 3D microstructure data are invaluable to the modeling community, where such data are currently lacking [35, 38].

4. High-energy Synchrotron X-ray Computed Microtomography (μCT)

High-energy synchrotron X-ray μCT is a powerful non-destructive technique used to rapidly reconstruct the internal structures of objects in 3D with a high spatial resolution. A box beam is used. Similar to HEDM, the sample rotates for 180 or 360° about an axis perpendicular to the incident beam, and images of the transmitted direct beam are collected downstream by a high-resolution area detector at small rotation steps, typically in a small fraction of a degree. Figure 3a shows the setup with an encapsulated radioactive material in the beam (in this particular case, an irradiated U-10Zr [39]). When performed at (partially to fully) coherent synchrotron sources, sample contrast can be selected to be dominated by absorption or phase by changing $L_{s\text{-}d}$ from near (several mms) to far (above cm). These mechanisms allow for excellent detectability of morphological features such as cracks, voids, or even secondary phases.

Thomas et al. [39] used μCT to study the porosity and phase regions in an irradiated U-10Zr fuel specimen of a volume of ~8×10^5 μm^3. They revealed the presence of three distinct phase regions correlating to different U content, namely U-poor, U-intermediate, and U-rich. The porosity and fuel swelling levels were determined, and the porosity distribution was further classified based on the pore volumes and morphology. The spatial correlation between the pores and the phase regions was also evaluated. This pioneering work paved the way for the high-end characterization of irradiated nuclear fuels and provided valuable information for improving fuel performance models.

High-energy synchrotron X-ray μCT has also been used by Wade-Zhu et al. to study the fracture of irradiated nuclear graphite during *in situ* compression (effectively a 4D study with time being the 4^{th} dimention) [40]. The authors used a small-scale load frame to perform staged compression tests on a radioactive graphite sample sealed in a double-encapsulated vessel, and the same setup was used to test the unirradiated counterpart. The processes of crack initiation, propagation and arrest were captured in both irradiated and unirradiated samples. It was found that the irradiated sample had enhanced crack tip blunting due to the expansion and the increased presence of macro-pores, which was a dominant toughening mechanism for graphite. The irradiated sample also showed a suppression of micro-cracking compared to the unirradiated counterpart. This novel study could provide valuable information to optimize nuclear graphite, and assist the development of computational models.

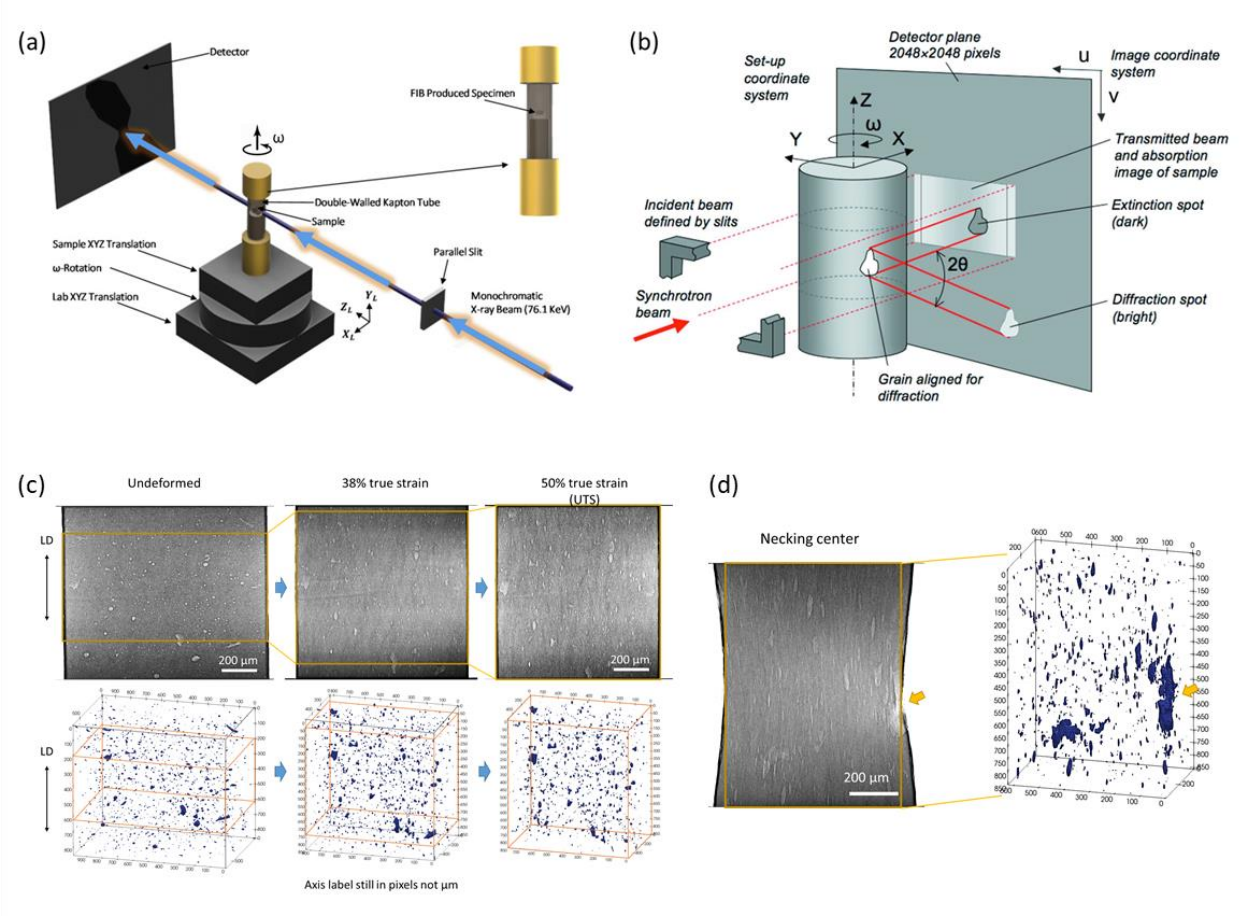

Figure 3. (a) Schematic showing the µCT setup for an irradiated material. Reproduced from Reference [39]. (b) Schematic showing the DCT setup. Reproduced from Reference [41] with permission of the International Union of Crystallography. (c) Top: X-ray radiographs of the gauge center region of an LPBF 316L sample, showing the morphology of the built-in pores at different deformation levels. Bottom: 3D tomography views of pores in the same regions as in (a), with the axis labels being in pixel and 1 pixel equaling 1.172 µm. The yellow boxed volumes outline the same volume that are consistently tracked throughout the deformation. (d) Left: the radiograph of the necking center showing the pores being severely deformed. Right: 3D tomography view of the pores, with the axis labels being in pixel and 1 pixel equaling 1.172 µm. In both figures, the yellow arrow points to a large pore approaching the surface. Subfigures (c) and (d) are reproduced from Reference [20].

Cracking also happens in structural materials, and a pertinent issue in reactor-related applications is the stress corrosion cracking (SCC). *In situ* synchrotron X-ray µCT has been employed by Schoell et al. [42] to understand the mechanisms behind chlorine-induced SCC (CISCC) in 304 stainless steel. The researchers installed a pre-cracked sample with $MgCl_2$ pre-deposition into a small Kapton chamber containing hot humid air, which was integrated to a custom-built tensile frame. Under a tensile load the crack propagated. The tomography scans at multiple deformation steps showed the branching of the crack in corrosive environment. Most of the branching occurred towards the surface of the sample, most likely due to a combination of the stress condition and the pitting on the surface.

Additively manufactured (AM) materials, which are of high interest to the nuclear materials community, are well-positioned to be studied with µCT since they typically contain built-in defects such as lack-of-fusion pores, thermal cracks, or inclusions that show contrasts with the matrix [43]. For example, we [20] studied the tensile deformation of a 316L stainless steel manufactured by LPBF using WAXS and

synchrotron X-ray μCT, and found that while the built-in pores co-deformed with the matrix material (Figure 3c) and did not have a significant role in plasticity, the near-surface pores might play a role in promoting the localized deformation (i.e. necking) (Figure 3d). We also imaged the pores in LPBF 316L stainless steel specimens before [44] and after (unpublished) creep deformation, which helped to explain the possible effect of the built-in pores on the creep life and ductility. A study by Carlton et al. [45] also provided direct evidence that the porosity distribution played a larger role in affecting the fracture mechanisms than the measured bulk density in tensile loading of a LPBF 316L stainless steel.

Another variant of high-energy X-ray μCT is diffraction contrast tomography (DCT) [41, 46]. Figure 3b illustrates the setup, which shows that the diffraction spots are acquired simultaneously (same detector) with the absorption image. DCT allows the reconstruction of 3D grain morphologies combined with their orientations in a polycrystalline sample, together with the reconstruction of the absorption contrast microstructure. Early in its development, DCT has been used to study the interaction between intergranular SCC and grain boundaries [47]. Recently, Fang et al. [48] used the technique and studied the bulk hydrides in a Zircaloy-2 slab. For the first time, the morphologies of the hydrides and the neighboring Zircaloy grains were reconstructed in 3D, the grain orientations were measured, and the normals of the hydride plates were determined. They found that the hydride in corn-flake shape grew past grain boundaries, with the plate normals clustered in the {0002} direction. The results could help in building realistic models for hydride precipitation and in developing predictive models for the Delayed Hydride Cracking.

5. Conclusion and outlook

Now is an exciting time in that new developments in HEX techniques, in particular in the *in situ* and 3D techniques, are matured at a number of synchrotron beamlines around the world, and pioneering studies have demonstrated their power in nuclear materials discovery. Being highly transmissible and non-destructive, these techniques are well suited for studying hazardous bulk nuclear materials, from irradiated graphite, to irradiated structural/cladding materials, to uranium fuel. The results provides deep insights into the microstructure-property correlations, and are promoting the development of high-fidelity computational models.

A trend is to combine multiple measurement modalities in one experiment to obtain the most comprehensive dataset in unprecedented detail. Increasingly, such multi-modal measurements are carried out *in situ* with mechanical and/or thermal loadings thanks to the deployment of many custom-made beamline apparatuses (for examples, see [4, 49]). One impressive study is on the crack propagation of a Ni-based superalloy during *in situ* cyclic loading by Naragani et al [50], which combined absorption contrast μCT, nf-HDEM and ff-HEDM to investigate crack growth on the grain-scale. Although this study was not specifically tuned for nuclear applications, the successful experimental design and the data analysis methodologies can be applied to nuclear materials research.

Developments are still ongoing and include efforts to streamline measurements on nuclear materials at existing or in-construction synchrotron beamlines. A notable effort, projected to come online by 2024, is the Activated Materials Laboratory (AML) [51] funded by the Nuclear Science User Facilities (NSUF). The AML will be constructed at Argonne National Laboratory adjacent to two new long beamlines associated with the APS-Upgrade project. The AML will facilitate a safe, robust and convenient handling of activated materials for X-ray experiments at the APS. On a different node, experimental and computational scientists are joining efforts in developing machining-learning-based fast data processing methodologies [52] aiming to provide real-time feedback on the materials status during the beamtime [private communications]. Currently, data analysis occurs post-beamtime in the majority of cases, which can take from days to years and is often very labor-intensive. Real-time and more streamlined data analysis

would help in the critical decision-making moments during *in situ* experiments when valuable nuclear materials are being measured, and also enable deeper analysis of large, multi-dimensional data.

Acknowledgements

This work was supported by the U.S. Department of Energy, Office of Nuclear Energy under Contract DE-AC02-06CH11357 with Argonne National Laboratory, managed and operated by UChicago Argonne LLC. The author would like to thank Dr. Jun-Sang Park at Argonne National Laboratory for help with figures, and thank Dr. Jonathan Almer and Dr. Yiren Chen at Argonne National Laboratory for reviewing the writing.

References

[1] S.J. Zinkle, G.S. Was, Materials challenges in nuclear energy, Acta Materialia 61(3) (2013) 735-758.
[2] P. Hosemann, Small-scale mechanical testing on nuclear materials: bridging the experimental length-scale gap, Scripta Materialia 143 (2018) 161-168.
[3] A. Prasitthipayong, Small-Scale Mechanical Testing and Size Effects in Extreme Environments, University of California, Berkeley, 2017.
[4] X. Zhang, C. Xu, L. Wang, Y. Chen, M. Li, J.D. Almer, E. Benda, P. Kenesei, A. Mashayekhi, J.-S. Park, F.J. Westferro, iRadMat: A thermo-mechanical testing system for in situ high-energy X-ray characterization of radioactive specimens, Review of Scientific Instruments 88(1) (2017) 015111.
[5] D.J. Sprouster, R. Weidner, S.K. Ghose, E. Dooryhee, T.J. Novakowski, T. Stan, P. Wells, N. Almirall, G.R. Odette, L.E. Ecker, Infrastructure development for radioactive materials at the NSLS-II, Nuclear Instruments and Methods in Physics Research Section A: Accelerators, Spectrometers, Detectors and Associated Equipment 880 (2018) 40-45.
[6] B. Sitaud, P.L. Solari, S. Schlutig, I. Llorens, H. Hermange, Characterization of radioactive materials using the MARS beamline at the synchrotron SOLEIL, Journal of Nuclear Materials 425(1) (2012) 238-243.
[7] Nuclear Science User Facilities. https://nsuf.inl.gov/).
[8] J. Tuszynski, PhotonAttenuation (https://www.mathworks.com/matlabcentral/fileexchange/12092-photonattenuation), MATLAB Central File Exchange, 2021.
[9] X. Zhang, C. Xu, Y. Chen, W.-Y. Chen, J.-S. Park, P. Kenesei, J. Almer, J. Burns, Y. Wu, M. Li, High-energy synchrotron x-ray study of deformation-induced martensitic transformation in a neutron-irradiated Type 316 stainless steel, Acta Materialia 200 (2020) 315-327.
[10] L. Wang, M. Li, J. Almer, Investigation of deformation and microstructural evolution in Grade 91 ferritic–martensitic steel by in situ high-energy X-rays, Acta Materialia 62 (2014) 239-249.
[11] D.J. Sprouster, J. Sinsheimer, E. Dooryhee, S.K. Ghose, P. Wells, T. Stan, N. Almirall, G.R. Odette, L.E. Ecker, Structural characterization of nanoscale intermetallic precipitates in highly neutron irradiated reactor pressure vessel steels, Scripta Materialia 113 (2016) 18-22.
[12] X. Zhang, M. Li, J.-S. Park, P. Kenesei, J. Almer, C. Xu, J.F. Stubbins, In situ high-energy X-ray diffraction study of tensile deformation of neutron-irradiated polycrystalline Fe-9%Cr alloy, Acta Materialia 126 (2017) 67-76.
[13] C. Xu, X. Zhang, Y. Chen, M. Li, J.-S. Park, P. Kenesei, J. Almer, Y. Yang, In-situ high-energy X-ray characterization of neutron irradiated HT-UPS stainless steel under tensile deformation, Acta Materialia 156 (2018) 330-341.
[14] T. Koyanagi, D.J. Sprouster, L.L. Snead, Y. Katoh, X-ray characterization of anisotropic defect formation in SiC under irradiation with applied stress, Scripta Materialia 197 (2021) 113785.

[15] N. Simos, P. Hurh, E. Dooryhee, L. Snead, D. Sprouster, Z. Zhong, H. Zhong, S. Ghose, Z. Kotsina, K. Ammigan, J. Hylen, V. Papadimitriou, R. Zwaska, D. Senor, A. Casella, D.J. Edwards, 120 GeV neutrino physics graphite target damage assessment using electron microscopy and high-energy x-ray diffraction, Physical Review Accelerators and Beams 22(4) (2019) 041001.
[16] F. Laliberte, M. Li, J. Almer, L. Liu, In-situ synchrotron X-ray study of microstructural evolution during creep deformation in Grade 91 steel, Materials Science and Engineering: A 737 (2018) 115-123.
[17] E. Vakhitova, D. Sornin, J. Wright, T. Tomida, M. François, In situ synchrotron analysis of phase transformation at high temperatures in ODS ferritic steel, Journal of Materials Science 55(13) (2020) 5600-5612.
[18] O.V. Shiman, T. Skippon, E. Tulk, M.R. Daymond, Strain evolution in Zr-2.5 wt% Nb observed with synchrotron X-ray diffraction, Materials Characterization 146 (2018) 35-46.
[19] Y. Miao, K. Mo, J.-S. Park, J. Almer, C. Massey, C. Havrilak, A.T. Nelson, H. Connaway, A.M. Yacout, In Situ Synchrotron Tensile Investigations on Ultrasonic Additive Manufactured (UAM) Zirconium, Argonne National Lab. (ANL), Argonne, IL (United States), 2021.
[20] X. Zhang, P. Kenesei, J.-S. Park, J. Almer, M. Li, In situ high-energy X-ray study of deformation mechanisms in additively manufactured 316L stainless steel, Journal of Nuclear Materials 549 (2021) 152874.
[21] D.J. Sprouster, E. Kardoulaki, R. Weidner, A.M. Raftery, M. Elbakhshwan, R. Pokharel, H.M. Reiche, D.D. Byler, S.K. Ghose, E. Dooryhee, K.J. McClellan, L.E. Ecker, In situ X-ray characterization of uranium dioxide during flash sintering, Materialia 2 (2018) 176-182.
[22] M.S. Elbakhshwan, S.K. Gill, A.T. Motta, R. Weidner, T. Anderson, L.E. Ecker, Sample environment for in situ synchrotron corrosion studies of materials in extreme environments, Review of Scientific Instruments 87(10) (2016) 105122.
[23] T.M. Copeland-Johnson, C.K.A. Nyamekye, S.K. Gill, L. Ecker, N. Bowler, E.A. Smith, R.B. Rebak, Characterization of Kanthal APMT and T91 oxidation at beyond design-basis accident temperatures, Corrosion Science 171 (2020) 108598.
[24] K. Mo, Y. Miao, R. Xu, T. Yao, J. Lian, L.M. Jamison, A.M. Yacout, Lattice strain mapping of cracks and indentations in UO2 using synchrotron microdiffraction, Journal of Nuclear Materials 529 (2020) 151943.
[25] J.-S. Park, J. Okasinski, K. Chatterjee, Y. Chen, J. Almer, Non-Destructive Characterization of Engineering Materials Using High-Energy X-rays at the Advanced Photon Source, Synchrotron Radiation News 30(3) (2017) 9-16.
[26] N. Simos, P. Nocera, Z. Zhong, R. Zwaska, N. Mokhov, J. Misek, K. Ammigan, P. Hurh, Z. Kotsina, Proton irradiated graphite grades for a long baseline neutrino facility experiment, Physical Review Accelerators and Beams 20(7) (2017) 071002.
[27] X. Zhang, J.-S. Park, J. Almer, M. Li, Characterization of neutron-irradiated HT-UPS steel by high-energy X-ray diffraction microscopy, Journal of Nuclear Materials 471 (2016) 280-288.
[28] X. Zhang, M. Li, J.-S. Park, P. Kenesei, H. Sharma, J. Almer, High-energy x-ray diffraction microscopy study of deformation microstructures in neutron-irradiated polycrystalline Fe-9%Cr, Journal of Nuclear Materials 508 (2018) 556-566.
[29] P.A. Shade, W.D. Musinski, M. Obstalecki, D.C. Pagan, A.J. Beaudoin, J.V. Bernier, T.J. Turner, Exploring new links between crystal plasticity models and high-energy X-ray diffraction microscopy, Current Opinion in Solid State and Materials Science 23(5) (2019) 100763.
[30] J.V. Bernier, R.M. Suter, A.D. Rollett, J.D. Almer, High-Energy X-Ray Diffraction Microscopy in Materials Science, Annual Review of Materials Research 50(1) (2020) 395-436.
[31] H.F. Poulsen, G.B.M. Vaughan, Multigrain crystallography and three-dimensional grain mapping, in: C.J. Gilmore, J.A. Kaduk, H. Schenk (Eds.), International Tables for Crystallography: Powder Diffraction, Wiley, New York, 2019, pp. 601-616.

[32] R. Pokharel, Overview of High-Energy X-Ray Diffraction Microscopy (HEDM) for Mesoscale Material Characterization in Three-Dimensions, in: T. Lookman, S. Eidenbenz, F. Alexander, C. Barnes (Eds.), Materials Discovery and Design: By Means of Data Science and Optimal Learning, Springer International Publishing, Cham, 2018, pp. 167-201.
[33] R.M. Suter, D. Hennessy, C. Xiao, U. Lienert, Forward modeling method for microstructure reconstruction using x-ray diffraction microscopy: Single-crystal verification, Review of Scientific Instruments 77(12) (2006) 123905.
[34] H. Abdolvand, M. Majkut, J. Oddershede, J.P. Wright, M.R. Daymond, Study of 3-D stress development in parent and twin pairs of a hexagonal close-packed polycrystal: Part I – in-situ three-dimensional synchrotron X-ray diffraction measurement, Acta Materialia 93 (2015) 246-255.
[35] H. Abdolvand, M. Majkut, J. Oddershede, J.P. Wright, M.R. Daymond, Study of 3-D stress development in parent and twin pairs of a hexagonal close-packed polycrystal: Part II – crystal plasticity finite element modeling, Acta Materialia 93 (2015) 235-245.
[36] J.P. Hanson, A. Bagri, J. Lind, P. Kenesei, R.M. Suter, S. Gradečak, M.J. Demkowicz, Crystallographic character of grain boundaries resistant to hydrogen-assisted fracture in Ni-base alloy 725, Nature Communications 9(1) (2018) 3386.
[37] R. Pokharel, D.W. Brown, B. Clausen, D.D. Byler, T.L. Ickes, K.J. McClellan, R.M. Suter, P. Kenesei, Non-Destructive Characterization of UO2+x Nuclear Fuels, Microscopy Today 25(6) (2017) 42-47.
[38] T.J. Turner, P.A. Shade, J.V. Bernier, S.F. Li, J.C. Schuren, P. Kenesei, R.M. Suter, J. Almer, Crystal Plasticity Model Validation Using Combined High-Energy Diffraction Microscopy Data for a Ti-7Al Specimen, Metallurgical and Materials Transactions A 48(2) (2017) 627-647.
[39] J. Thomas, A. Figueroa Bengoa, S.T. Nori, R. Ren, P. Kenesei, J. Almer, J. Hunter, J. Harp, M.A. Okuniewski, The application of synchrotron micro-computed tomography to characterize the three-dimensional microstructure in irradiated nuclear fuel, Journal of Nuclear Materials 537 (2020) 152161.
[40] J. Wade-Zhu, R. Krishna, A.J. Bodey, M. Davies, N.K. Bourne, C. Rau, B. Davies, A. Tzelepi, A.N. Jones, B.J. Marsden, P.M. Mummery, 4D synchrotron X-ray microtomography of fracture in nuclear graphite after neutron irradiation and radiolytic oxidation, Carbon 168 (2020) 230-244.
[41] G. Johnson, A. King, M.G. Honnicke, J. Marrow, W. Ludwig, X-ray diffraction contrast tomography: a novel technique for three-dimensional grain mapping of polycrystals. II. The combined case, Journal of Applied Crystallography 41(2) (2008) 310-318.
[42] R. Schoell, L. Xi, Y. Zhao, X. Wu, Z. Yu, P. Kenesei, J. Almer, Z. Shayer, D. Kaoumi, In situ synchrotron X-ray tomography of 304 stainless steels undergoing chlorine-induced stress corrosion cracking, Corrosion Science 170 (2020) 108687.
[43] X-Ray Microcomputed Tomography in Additive Manufacturing: A Review of the Current Technology and Applications, 3D Printing and Additive Manufacturing 5(3) (2018) 227-247.
[44] M. Li, X. Zhang, W.-Y. Chen, T.S. Byun, Creep behavior of 316 L stainless steel manufactured by laser powder bed fusion, Journal of Nuclear Materials 548 (2021) 152847.
[45] H.D. Carlton, A. Haboub, G.F. Gallegos, D.Y. Parkinson, A.A. MacDowell, Damage evolution and failure mechanisms in additively manufactured stainless steel, Materials Science and Engineering: A 651 (2016) 406-414.
[46] W. Ludwig, P. Reischig, A. King, M. Herbig, E.M. Lauridsen, G. Johnson, T.J. Marrow, J.Y. Buffière, Three-dimensional grain mapping by x-ray diffraction contrast tomography and the use of Friedel pairs in diffraction data analysis, Review of Scientific Instruments 80(3) (2009) 033905.
[47] A. King, G. Johnson, D. Engelberg, W. Ludwig, J. Marrow, Observations of Intergranular Stress Corrosion Cracking in a Grain-Mapped Polycrystal, Science 321(5887) (2008) 382-385.
[48] Q. Fang, M.R. Daymond, A. King, Study on the morphology of bulk hydrides by synchrotron X-ray tomography, Materials Characterization 134 (2017) 362-369.

[49] P.A. Shade, B. Blank, J.C. Schuren, T.J. Turner, P. Kenesei, K. Goetze, R.M. Suter, J.V. Bernier, S.F. Li, J. Lind, U. Lienert, J. Almer, A rotational and axial motion system load frame insert for in situ high energy x-ray studies, Review of Scientific Instruments 86(9) (2015) 093902.
[50] D.P. Naragani, P.A. Shade, P. Kenesei, H. Sharma, M.D. Sangid, X-ray characterization of the micromechanical response ahead of a propagating small fatigue crack in a Ni-based superalloy, Acta Materialia 179 (2019) 342-359.
[51] Starting a new era of nuclear innovation with Argonne's Activated Materials Lab. https://www.ans.org/news/article-3176/starting-a-new-era-of-nuclear-innovation-with-argonnes-activated-materials-lab/, 2021).
[52] A. Tekawade, B. Sforzo, K. Matusik, A. Kastengren, C. Powell, High-fidelity geometry generation from CT data using convolutional neural networks, SPIE2019.